Available online at www.sciencedirect.com

SciVerse ScienceDirect

Ceramics International 39 (2013) 801–812

CERAMICS INTERNATIONAL

www.elsevier.com/locate/ceramint

Fabrication and characterization of micro-arc oxidized fluoride containing titania films on Cp Ti

K. Venkateswarlu[a,b], N. Rameshbabu[a,*], D. Sreekanth[a], A.C. Bose[b], V. Muthupandi[a], S. Subramanian[c]

[a]Department of Metallurgical and Materials Engineering, National Institute of Technology, Tiruchirappalli 620015, Tamilnadu, India
[b]Department of Physics, National Institute of Technology, Tiruchirappalli 620015, Tamilnadu, India
[c]Department of Materials Engineering, Indian Institute of Science, Bangalore 560012, Karnataka, India

Received 24 April 2012; received in revised form 16 June 2012; accepted 2 July 2012
Available online 10 July 2012

Abstract

The present study is focussed at establishing an appropriate electrolyte system for developing electrochemically stable and fluorine (F) containing titania (F-TiO_2) films on Cp Ti by micro-arc oxidation (MAO) technique. To fabricate the F-TiO_2 films on Cp Ti, different electrolyte solutions of chosen concentrations of tri-sodium orthophosphate (TSOP, $Na_3PO_4 \cdot 1_2H_2O$), potassium hydroxide (KOH) and various F-containing compounds such as ammonium fluoride (NH_4F), potassium fluoride (KF), sodium fluoride (NaF) and potassium fluorotitanate (K_2TiF_6) are employed. The structural and morphological characteristics, thickness and elemental composition of the developed films have been assessed by X-ray diffraction (XRD), scanning electron microscopy (SEM) and energy dispersive spectroscopy (EDS) techniques. The in-vitro electrochemical corrosion behavior of the films was studied under Kokubo simulated body fluid (SBF) environment by potentiodynamic polarization, long term potential measurement and electrochemical impedance spectroscopy (EIS) methods. The XRD and SEM-EDS results show that the rutile content in the films vary in the range of 15–37 wt% and the F and P contents in the films is found to be in the range of 2–3 at% and 2.9–4.7 at% respectively, suggesting that the anatase to rutile phase transformation and the incorporation of F and P into the films are significantly controlled by the respective electrolyte solution. The SEM elemental mapping results show that the electrolyte borne F and P elements are incorporated and distributed uniformly in all the films. Among all the films under study, the film developed with 5 g TSOP + 2 g KOH + 3 g K_2TiF_6 electrolyte system exhibits considerably improved in-vitro corrosion resistance and therefore best suited for biomedical applications.

Keywords: A. Films; C. Corrosion; D. TiO_2; E. Biomedical applications

1. Introduction

Ti and Ti based alloys are extensively being used in orthopaedic and dental applications because of their non-toxicity, biocompatibility, corrosion resistance and good mechanical properties such as high strength, durability and light weight [1]. The good corrosion resistance and biocompatibility of these materials are attributed to a thin oxide film formed naturally on the implant surface when exposed to air and/or moisture at room temperature. However these materials, when implanted for dental and orthopaedic applications, are prone to be affected by bacterial infection caused by the growing bacterial plaque on the implant surface. It has been reported that microbial plaque accumulation around the implant surface may increase the risk of bacterial infection and further develop into peri-implantitis, accompanied with tissue destruction and even bone loss [2].

In order to reduce the probability of implant-associated infections during surgery and healing process, extensive research on Ti implant materials possessing anti-bacterial activity has been undertaken. Liu et al. [2,3] have reported that fluoride ion incorporated Ti implant surface showed improved antibacterial activity and biocompatibility compared

*Corresponding author. Tel.: +91 431 2503464; fax: +91 431 2500133.
E-mail addresses: rameshrohith@gmail.com, nrb@nitt.edu (N. Rameshbabu).

0272-8842/$36.00
http://dx.doi.org/10.1016/j.ceramint.2012.07.001

to that of the bare Ti implant surface. Similarly Cooper et al. [4] have shown that fluoride ion treatment of TiO_2 grit-blasted titanium substrates enhanced osteoblastic differentiation of human mesenchymal stem cells and significantly increased the bone-to-implant contact in the rat tibia model. Further, it has been reported that dental implants with fluoride-modified titanium dioxide showed improved bone response and clinical performance by inducing topographical changes at the nanoscale level and incorporating fluoride ions in the surface structure. Consequently, fluoride is considered to play a role in the chemical bonding between the newly formed bone and the modified dental implant surface [5]. Similarly Ellingsen found that NaF-treated Ti implants showed greater retention in bone compared to non-treated Cp titanium. He also suggested that the presence of a fluoride coat on the titanium implant surface stimulates the bone response leading to a connection between titanium and phosphate from body fluids. In addition, he proposed that the free fluoride ions will catalyze this reaction and induce the formation of fluoridated hydroxyapatite in the surrounding bone [6]. Hence from the reported literature it can be inferred that the presence of fluoride in the Ti implant surface can make the implant best suited for both dental and orthopaedic applications.

However, the application of NaF coat directly on to the implant surface is detrimental to its corrosion resistance and limits its long term applications [7]. Hence a comparatively successful implant material should be capable of withstanding long term biological corrosion as well as preventing the implant from infections. Therefore, the development of corrosion resistant titania films containing a significant amount of fluoride in its surface layer can serve the purpose of a successful implant material. Micro-arc oxidation (MAO) is a relatively convenient and effective technique to develop thick, adherent, corrosion and wear resistant films on the surfaces of Ti, Mg, Al and their alloys [8–10]. In addition, the technique can also introduce various desired elements into the MAO films and produce various functional films with a porous structure [11,12]. With the above objectives in mind, in the present study, the corrosion resistant and fluoride containing titania films were developed on CpTi by MAO technique with different electrolyte solutions comprising of various fluoride containing compounds such as NH_4F, KF, NaF and K_2TiF_6. Further, a comparative study of the effect of the various fluoride containing electrolyte solutions on the structural, morphological and corrosion characteristics of titania films was performed and thereby an appropriate electrolyte system for fabricating corrosion resistant titania films was optimized.

2. Experimental

2.1. Fabrication of MAO films

The test coupons for the MAO treatment were prepared as mentioned in our previous work [13]. The MAO experiments were conducted with 4 different electrolyte systems consisting of decisively chosen concentrations of tri-sodium orthophosphate (TSOP, $Na_3PO_4 \cdot 12H_2O$), potassium hydroxide (KOH), ammonium fluoride (NH_4F), potassium fluoride (KF), sodium fluoride (NaF) and potassium fluorotitanate (K_2TiF_6). The conductivity of the prepared electrolyte solutions was measured by an ECtestr11+ (Oakton Instruments, Singapore) multi-range conductivity meter. The compositions of the four electrolytes employed in the present study are shown in Table 1. All the chemicals used were obtained from Merck India Pvt. Ltd. A stainless steel bowl of 15 cm diameter containing the electrolyte solution was used as cathode and the test coupons immersed in the electrolytes served as anode. A DC power supply unit (Milman Thin Films Pvt. Ltd, Pune, India) with a maximum peak voltage of 900 V and a maximum output current of 15 A was employed to carry out the MAO process. All the samples were treated for 8 min at a constant current of 1 A corresponding to a current density of about 150 mA/cm^2. The electrolyte bath was water cooled during the process to maintain the bath temperature close to the room temperature to avoid thermally driven growth process. The electrolyte solution was kept under continuous stirring during the process by a digital magnetic stirrer [Q 20A, REMI, India] to ensure uniform electrolyte concentration and dissipation of heat generated. The breakdown voltage corresponding to each electrolyte system was recorded by a careful observation of the appearance of the initial micro-spark on the anodic surface. This was triplicated and the average values are reported in the present study. Similarly the final voltages observed at the end of 8 min processing time were also recorded. After the MAO treatment, the samples were cleaned with distilled water and air dried at room temperature. The identification codes for the MAO treated samples with their respective electrolyte composition, final voltage, relative amounts of anatase and rutile and the respective film thickness values obtained are presented in Table 1. The MAO treated samples are further referred to with these identification codes and the substrate is referred to as "S".

Table 1
Identification codes for the MAO films with their respective electrolyte systems, final voltage values, phase contents and coating thickness.

Sample code	Electrolyte composition	V_f (V)	Film thickness ±1 (μm)	Anatase (wt%)	Rutile (wt%)
NF	5 g TSOP +3 g NH_4F +2 g KOH	425	11	80.1	19.9
KF	5 g TSOP +3 g KF +2 g KOH	406	13	69.9	30.1
NaF	5 g TSOP +3 g NaF +2 g KOH	390	15	64.4	35.6
KTF	5 g TSOP +3 g K_2TiF_6 +2 g KOH	431	10	62.7	37.3

2.2. Morphology, elemental composition and phase analysis of MAO films

The surface morphology, thickness and the elemental composition of the test samples were assessed using a Hitachi-S3000N scanning electron microscope equipped with energy dispersive spectroscopy (EDS) facility. The phase composition of the prepared films was analyzed by a Rigaku X-ray diffractometer (Ultima III, Rigaku, Japan) using Cu Kα radiation at 40 kV and 30 mA over a 2θ range of 20°–60° with a scan speed of 1°/min and a step size of 0.05°.

2.3. In-vitro electrochemical corrosion study

The in-vitro electrochemical corrosion characteristics of the substrate and the MAO films were studied under SBF conditions (7.4 pH and 37 °C) by both potentiodynamic polarization and electrochemical impedance spectroscopy (EIS) tests using fresh samples for each of these tests. The SBF test medium of pH 7.4 was prepared following the procedure suggested by Kokubo et al. [14]. A computer controlled corrosion testing unit (Gill AC, ACM Instruments, UK) was used to obtain the polarization and EIS plots and a three electrode cell, with sample as working electrode, saturated calomel electrode (SCE) as reference electrode and platinum foil as counter electrode, was employed in the present study. All the experiments were conducted in aerated conditions and the SBF medium was kept under continuous *stirring* during the tests. An exposed area of 0.5 cm^2 was kept in contact with the test solution during the test. Prior to these tests all the samples (S, NF, KF, NaF and KTF) were immersed in the test solution for 4 h to attain a stable open circuit potential (OCP). The OCP measurements were conducted for every 5 min during the immersion time of 4 h. The cathodic and anodic Tafel constants (β_c and β_a), corrosion current density (j_{corr}) and corrosion rate of the films were obtained from the Tafel extrapolation method of the Tafel plots obtained, over a potential range of ±200 mV with reference to OCP employing a scan rate of 0.166 mV/s [15]. Similarly, the passivation behavior of the films in the test solution was studied over a potential range of −500 mV to 3000 mV by performing potentiodynamic polarization tests. The polarization resistance (R_p) of all the test samples was calculated using the Stern–Geary equation [16]

$$R_p = \frac{\beta_a \times \beta_c}{2.303 j_{corr}(\beta_a + \beta_c)} \quad (1)$$

In addition, the frequency response of the fabricated films was also tested by EIS studies over a frequency range of 10^{-2} Hz–100 kHz by applying a small perturbation AC signal with amplitude of ±10 mV. The obtained EIS data was analyzed by curve fitting and circuit modeling using ZView® software.

3. Results and discussion

3.1. Voltage–time (V–T) response characteristics

The *V–T* response curves of the MAO process for the four electrolyte systems employed in the present study are depicted in Fig. 1. Based on the difference in the process voltage rising rate and sparking behavior, the whole film growth process can be mainly divided into three stages namely the anodic oxidation stage (up to breakdown voltage), the dynamic MAO (sparking) stage and the near steady state MAO (arcing) stage. In the anodic oxidation stage the process voltage increases linearly at a very high rate to maintain the initially set current value. In this stage, a thin transparent barrier film forms at the interface of anode and electrolyte with no apparent sparks on the anodic surface as follows:

$$Ti^{4+} + 2OH^- + 2H_2O \rightarrow TiO_2 + 2H_3O^+ + 4e^- \quad (2)$$

The above equation suggests that the anodic film formation requires the Ti metal dissolution. The electrolyte conductivity and breakdown voltage (V_b) values corresponding to each electrolyte solution are shown in Fig. 2. It is evident from Fig. 2 that the electrolyte conductivity and the breakdown voltage for each electrolyte solution are inversely related. This trend is in accordance with the theoretical model proposed by Ikonopisov for the breakdown caused by an avalanche of electron injection into the oxide conduction band at the electrolyte/oxide interface [17]. According to this model, the breakdown voltage (V_B) and the electrolyte conductivity (κ) for a given electrolyte solution are related by the following Eq. (3)

$$V_B = a_B + b_B \log(1/\kappa) \quad (3)$$

where a_B and b_B are constant values for a given metal and electrolyte composition. The decrease in breakdown voltage with an increase in the electrolyte conductivity is due to the increase of incorporation rate of electrolyte anionic

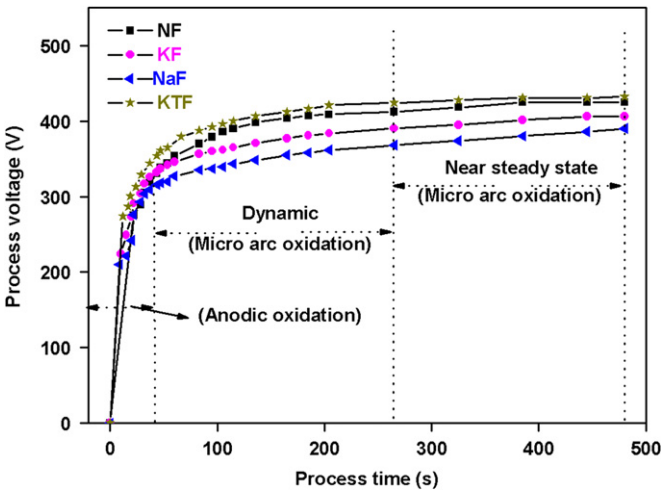

Fig. 1. Voltage–time response curves during MAO process of NF, KF, NaF and KTF films.

species such as OH^- into the oxide film which subsequently results in a higher density of primary electrons that is injected into the conduction band of the oxide. This higher primary electron current density subsequently results in reaching the critical value of the secondary electron current density at comparatively lower voltages and film breakdown occurs soon [18]. Thus the observed lowest breakdown voltage for the NaF film and the highest breakdown voltage for the KTF (~NF) film are justified as per their electrolyte conductivities measured and shown in Fig. 2.

In the second stage, during dynamic MAO, the *V–T* curves exhibited a sharp decrease in their slope due to the occurrence of small and dense micro-sparks associated with the electron current. In the first stage, during anodic oxidation, the current passed through the grown oxide film could be represented by the ionic current only, whereas in the second stage, during dynamic MAO, both ionic species and electrons contribute to the current. Thus the total current should be represented by the sum of the ionic current and the electronic current caused by the sparking. Hence, a relatively low voltage is sufficient to maintain the same current value compared with the first stage. This results in a rapid fall in the rising rate of process voltage in the second stage.

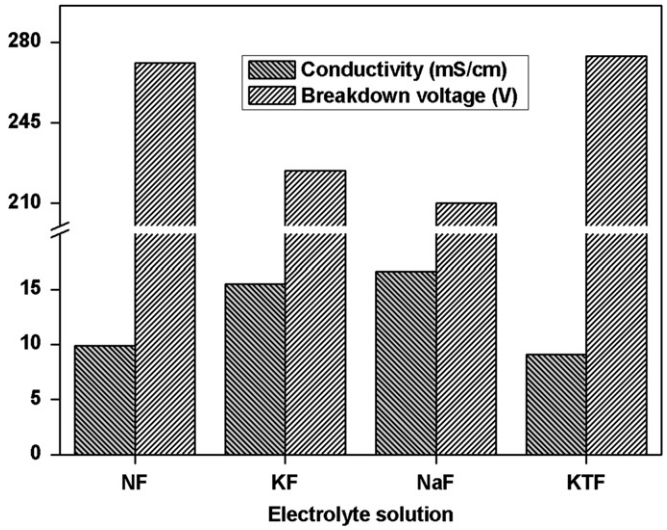

Fig. 2. Electrolyte conductivity and breakdown voltages for NF, KF, NaF and KTF electrolyte solutions.

In the third stage, during near steady state MAO, the anodic voltages reached a relatively stable value with a *V–T* curve slope close to 0 V/s attesting to the fact that no further increase in anodic voltage is required to maintain the same current value. This may be attributed to the significant increase in the fraction of the electronic current associated with the dielectric breakdown and constant resistance of the film due to the variation of the composition or structure of the film [19]. Thus the addition of various fluoride containing compounds to the reference electrolyte solution could affect the MAO process characteristics significantly.

3.2. Morphological studies

Fig. 3 shows the surface morphologies of NF, KF, NaF and KTF MAO films where all the films exhibit a common characteristic feature of a porous network structure. However, the surface morphologies of all the films differ significantly with respect to the pore features. In our

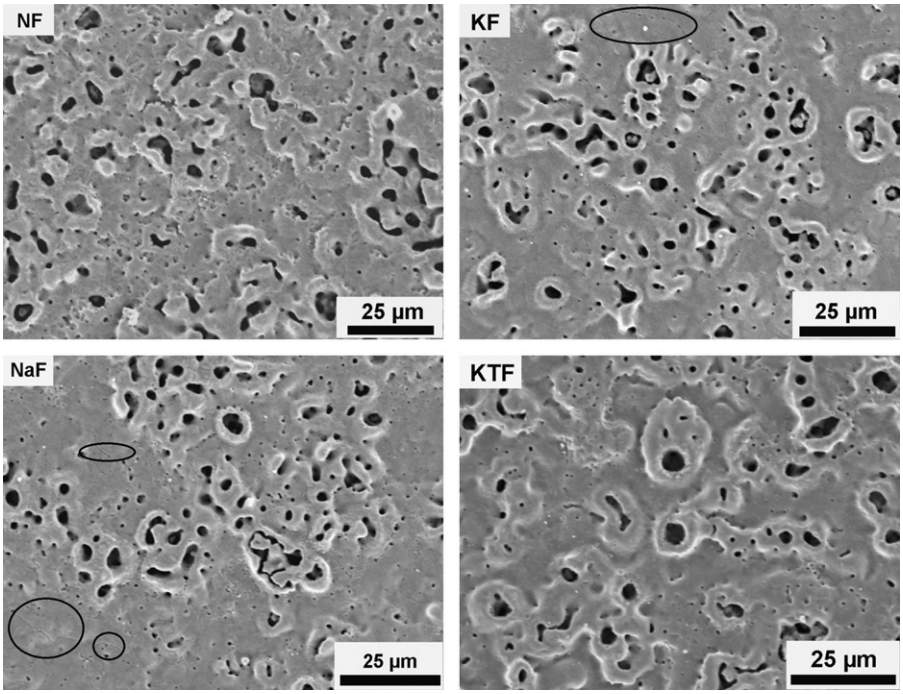

Fig. 3. SEM surface micrographs of NF, KF, NaF and KTF films.

previous study [20], we observed that the morphological features such as the nature (closed or opened or interconnected), size and number of pores over the surfaces of MAO films can be related to the nature (isolated or interconnected), size and number of micro-spark discharges occurred during the film growth process. Further we noticed that the *density* of the micro-spark discharges is mainly controlled by the *conductivity* of the employed electrolyte solution and these two are observed to be in direct relation with each other. In the present study it could be observed that, for the same treatment time, the surface of KTF film exhibited comparatively less number of pores due to the less micro-spark discharge density ensued from its lower electrolyte conductivity (as measured and shown in Fig. 2). In addition, the surface of KTF film looks more compact with well dispersed oxidation products thereby forming a pancake like structure [21] which closes the surrounding pores. On the other hand, for the same treatment time, the surface morphologies of KF and NaF films are similar and have more number of pores compared to that of KTF film, which is due to the higher micro-spark discharge density resulted by their higher electrolyte conductivities. In addition, the pores over the surfaces of KF and NaF films exhibit a moderate interconnectivity due to the inter-connected micro-spark discharges occurred during the process. Further the surfaces of KF and NaF films exhibited thermal stress driven micro-cracks, indicated by the black circles in Fig. 3, resulting from the rapid quenching of the oxidation products. Similarly, in spite of lower conductivity (less spark density) of its electrolyte solution, the surface of NF film apparently shows a larger number of fine and coarse pores compared to that of KF and NaF films which may be attributed to the insignificant dispersing nature of the oxidation products that left the existed pores unclosed. Consequently, the surface of NF seems less compact due to its higher pore size and density compared to the others. Thus the different surface morphologies of the films fabricated using different electrolyte solutions comprising of various fluoride containing compounds may be related to the dissimilar characteristics such as the density, intensity, size, number of micro-sparks and the dispersing nature of the oxidation products occurring during the MAO process.

3.3. Film thickness measurement

The values of the thickness of the NF, KF, NaF and KTF films measured from SEM cross-sectional analysis are reported in Table 1. It could be noticed that for the same treatment time the thickness of the films is decreasing in the order NaF > KF > NF > KTF suggesting that the nature of the fluoride containing compound in the respective electrolyte solution has a marked influence on the film growth rate. The final thickness of a film is determined by the dominance of "anodic dissolution rate" or "film formation rate" during the MAO process. As evidenced from Eq. (2), the formation of anodic film is a consequence of the reaction between the Ti^{4+} ions and anions such as OH^- existing in the electrolyte solution. Therefore, the film formation requires the anodic dissolution to provide metal ions for subsequent reactions with the anions leading to the film formation. The "rate of anodic dissolution" and the "rate of film formation" are two opposing factors which reversely influence the final thickness of the film. In effect the film starts to grow in thickness as the rate of the film formation gets higher than the dissolution rate of the anode [22]. Thus the obtained trend in the thickness of the films (NaF > KF > NF > KTF) is attributed to their dominant film formation rates rather than that of their anodic dissolution rates. Further, the dominant anodic dissolution rate of the films is inversely related to their respective electrolyte conductivities (shown in Fig. 2). In other words, among the employed electrolytes, the one with higher electrolyte conductivity resulted in comparatively lower anodic dissolution rate. Thus among the NF, KF, NaF and KTF films the highest thickness of NaF and the lowest thickness of KTF films are in accordance with their highest and lowest electrolyte conductivities. Thus it can be concluded that the film formation rate of the MAO films can be tailored by selecting an electrolyte solution comprising of a suitable fluoride containing compound.

3.4. Compositional analysis

Apart from Ti and O, the chemical composition of the MAO films also includes the anionic species such as PO_4^{3-} and F^- derived from the electrolyte that could be incorporated during the film growth process. These ionic species can remain as such in non-crystalline form or can form complex phases with the metal ions during the course of MAO treatment time. Since, the properties of the MAO films strongly depend on their chemical composition, their determination will be helpful for a better understanding of its properties. Fig. 4 depicts the SEM-EDX spectra and the respective elemental mapping results obtained from the EDS analysis conducted on the substrate and NF, KF, NaF and KTF treated MAO films. It can be observed from Fig. 4 that the boxes, showing the mapping of F and P present in the substrate, showed only a dark back ground indicating the absence of F and P. On the other hand, all the MAO films consisted of F and P in addition to O and Ti. The presence of F and P in the developed films demonstrates that the electrolyte species enter the discharge channels during the film growth process. In addition, it is evident from the EDX spectra and elemental mapping results for the element 'P' in Fig. 4, that the incorporation of 'P' into the film is significantly controlled by the respective electrolyte solution. The addition of KF and NaF inhibited the 'P' incorporation while the addition of NF and KTF promoted the 'P' incorporation into their respective films. Thus the content of the element 'P' in the films is decreased in the order KTF > NF > KF > NaF indicating that the extent of incorporation of 'P' strongly

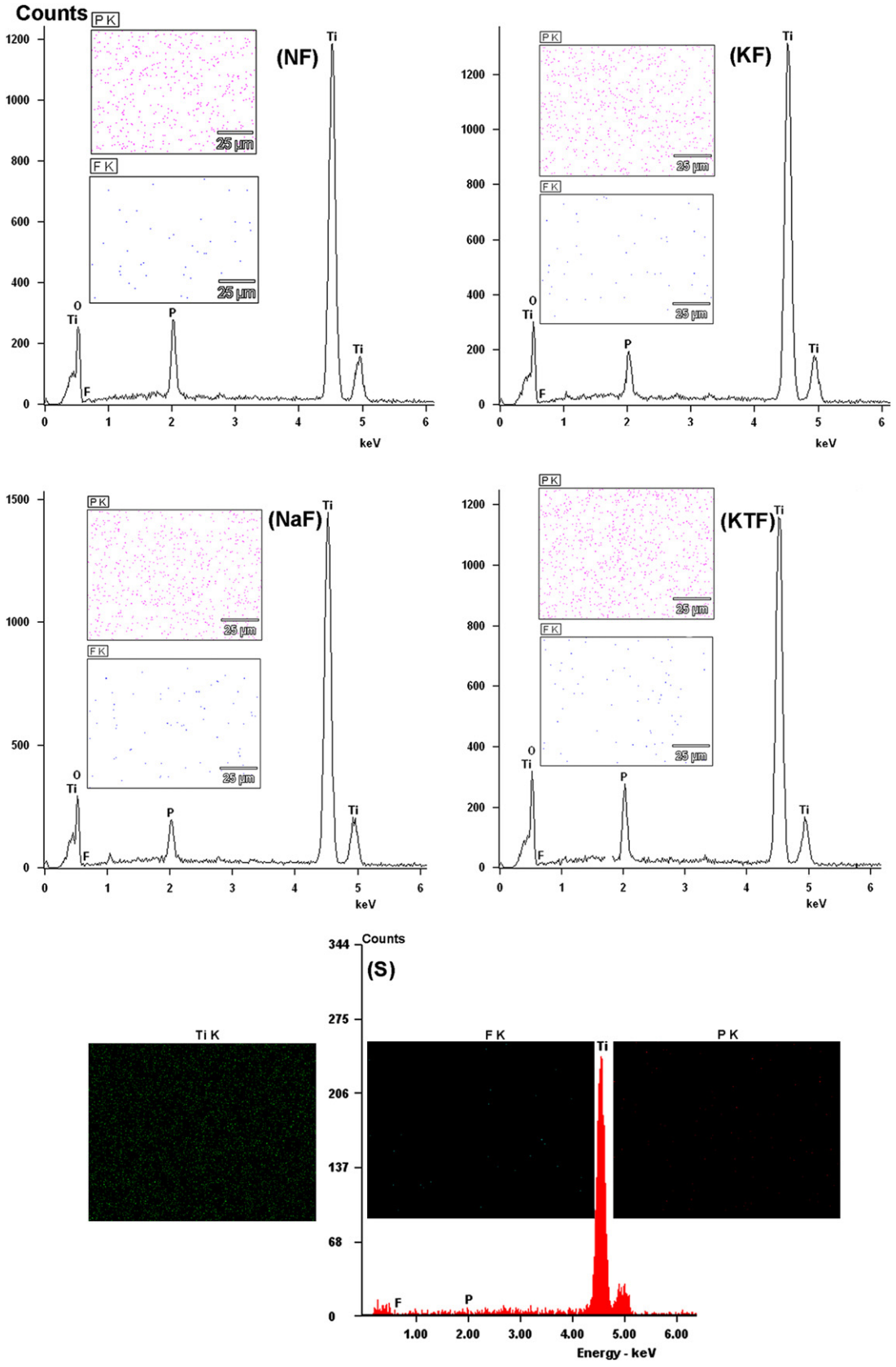

Fig. 4. SEM-EDX spectra and elemental mapping results of substrate and NF, KF, NaF and KTF films.

depends on the conductivity of the respective electrolyte. The probability of the incorporation of electrolyte elements is decreased with increasing electrolyte conductivity or by processing at lower voltages. This is in accordance with the reported fact that high processing voltages employed during MAO process result in large discharges, which can sinter more elements arising from the electrolyte into the film [23]. Thus the content of electrolyte borne elements in the films is attributed to the process voltages employed during the film growth process. In addition, the elemental mapping results shown in Fig. 4 suggest that the electrolyte borne F and P elements are uniformly distributed over the surface of the films. Though the SEM elemental analysis results show a significant amount of 'P' especially in the films of NF and KTF, no phosphate containing phases are found in the XRD results, as discussed below, confirming that either it remains in amorphous form or the crystalline content is below the detection limit of XRD.

3.5. Phase analysis

The XRD patterns of the Cp Ti substrate (S) and the NF, KF, NaF and KTF films are shown in Fig. 5. In addition to the substrate diffraction peaks, the XRD patterns of all the MAO films exhibit the characteristic peaks of both anatase (at $2\theta \sim 25.3^{\circ}$, JCPDS no: 21-1272) and rutile (at $2\theta \sim 27.7^{\circ}$, JCPDS no: 21-1276) forms of TiO_2. A variation in the area under the characteristic diffraction peaks of anatase and rutile can be observed from the XRD patterns of the MAO films depicted in Fig. 5. This indicates that the phase transformation from the metastable anatase to the stable rutile phase occurs at different rates based on the nature of the fluoride containing compound present in the electrolyte solution. This can be attributed to the variations in the micro-spark discharge characteristics such as spark frequency, density and intensity during the respective film growth process. The weight

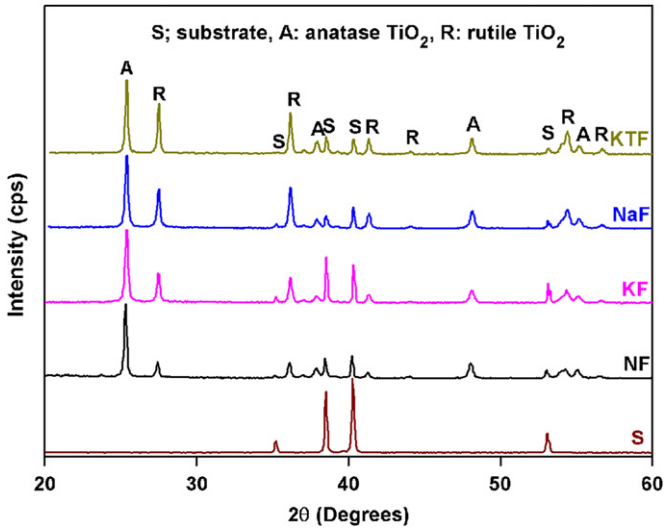

Fig. 5. XRD patterns of the NF, KF, NaF and KTF films.

fractions of the anatase and rutile phases in the respective film were determined by considering the intensities of the characteristic peaks of each oxide phase in the XRD patterns. The relative amounts of anatase (X_A) and rutile (X_R) in the fabricated films as calculated by the following formula [24] are given in Table 1.

$$X_R = \frac{1}{1+0.8(I_A/I_R)} \text{ and } X_A = 1-X_R \quad (4)$$

where I_A and I_R are the characteristic peak intensities of anatase (101) and rutile (110), respectively. It can be seen from Table 1 that the rutile content in the film is 19.9%, 30.1%, 35.6% and 37.3% for NF, KF, NaF and KTF, respectively. This result confirms the possibility of developing an 'F' containing titania film with appropriate contents of anatase and rutile phases by employing an electrolyte solution comprising of a suitable F-containing compound. However, among the films the rate of anatase to rutile phase transformation decreases in the order KTF > NaF > KF > NF. This is due to the variations in the film forming voltages and the electrolyte conductivities which subsequently result in different micro-spark discharge characteristics and thermal gradients across the thickness of the films. In other words, higher the film forming voltage more is the *intensity* of the sparks in the discharge channels and thereby more is the sparking energy that results in a higher local temperature that promotes the transformation from the metastable anatase phase to the thermodynamically stable rutile phase. Similarly, higher the electrolyte conductivity more is the *density* of the micro-sparks that result in a lower thermal gradient through the grown oxide film, which in turn leads to a local flux concentration that promotes further phase transformation. Thus the spark discharge characteristics and the low thermal conductivity of the oxide film could be responsible for the anatase to rutile phase transformation at different rates during the process. The formation of an initial amorphous oxide film and its conversion to crystalline anatase form and its subsequent transformation to a thermodynamically stable rutile phase is reported elsewhere [25].

3.6. In-vitro electrochemical corrosion characteristics

In the present study, the corrosion characteristics of the developed films in Kokubo's SBF medium were analyzed based on the thermodynamic as well as the kinetic information obtained by performing OCP or corrosion potential (E_{corr}) measurement tests and Tafel analysis tests respectively. In addition, the passivation behavior of the films was studied over a potential range of −500 to 3000 mV Vs SCE by performing the potentiodynamic polarization tests. To describe the corrosion mechanism of the MAO films, EIS tests were performed and the obtained data were analyzed by curve fitting and equivalent circuit modeling.

3.6.1. OCP measurements (thermodynamic studies)

The OCP is a parameter that indicates the thermodynamic tendency of an electrode to undergo electrochemical reactions in a corrosive medium. The higher the OCP of a working electrode, lesser is its tendency to participate in the electrochemical reactions. Fig. 6 shows the OCP curves for the substrate and the MAO films recorded for every 5 min during an immersion time of 4 h in SBF test medium and the corresponding values are reported in Table 2. As can be observed from Fig. 6 and Table 2, the OCP values of all the MAO films are shifted considerably in the noble direction compared to that of the substrate indicating their higher thermodynamic stability, consequent to their participation in the electrochemical reactions. However, the OCP curves of the substrate and the MAO films exhibit different features during the immersion time of 4 h. For example, initially the OCP of the substrate increases linearly and reaches a stable potential of −42.6 mV after an immersion time of about 40 min and continues to remain stable over the remaining immersion time. This can be attributed to the formation of a thin and adherent film at the metal/solution interface. On the other hand, initially the OCP of NF film increases linearly due to the formation of a thin oxide film at the metal/oxide interface and reach a maximum OCP value of about 203 mV over an immersion time of 20 min. Subsequently, it again decreases and reaches a comparatively stable potential of 35.3 mV after an exposure time of nearly 3 h. This subsequent decrease in OCP over an immersion time of 20 min–3 h can be attributed to the increased activity [26] due to the defective nature of the newly formed oxide film at the metal/oxide interface. Further, the steady behavior of OCP over the remaining immersion time (3–4 h) can be ascribed to the stable nature exhibited by the formed oxide film. Likewise the OCPs of KF and NaF increase slowly and reach their respective stable potentials of 67.9 and 93.8 mV, respectively after an immersion time of 3 h and remain unchanged during the remaining immersion time. In contrast to the OCP trends shown by all the other films, the OCP of KTF exhibits almost a constant higher OCP value of 136.4 mV after an immersion time of 35 min and remains unaltered over the remaining period of immersion. It can be observed that all the MAO films attain a stable OCP value after an immersion time of 3 h and continue to exhibit almost the same value up to 4 h. It can be inferred from the OCP results that the thermodynamic tendency of the MAO films towards the electrochemical oxidation reaction follows the sequence; S > NF > KF > NaF > KTF. Thus it can be concluded that the KTF film has shown more passive behavior towards the anodic reactions compared to the other films.

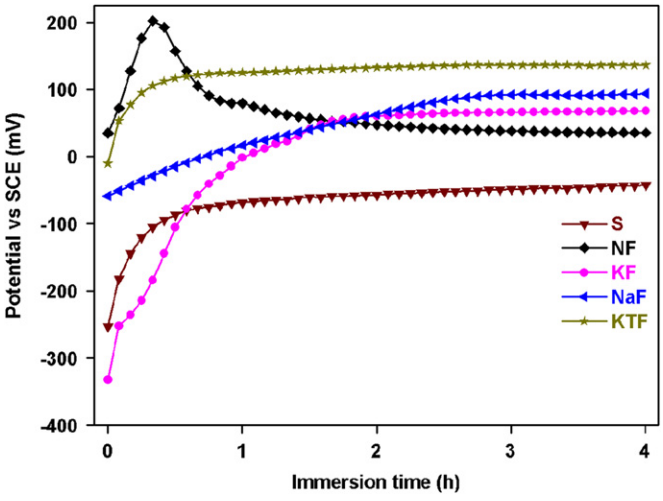

Fig. 6. OCP curves of the NF, KF, NaF and KTF films for an immersion period of 4 h.

3.6.2. Tafel analysis (kinetic studies)

The Tafel plots of the substrate and the MAO films obtained over a potential range of ±200 mV with reference to their stable OCP are shown in Fig. 7. The cathodic and anodic Tafel constants (β_c and β_a), the corrosion potential (E_{corr}), the corrosion current density (j_{corr}) and the corrosion rate of the substrate and the films derived by the Tafel extrapolation method for KTF film as an example, are shown in Fig. 8. Thus kinetic parameter values so obtained are reported in Table 2. It is noteworthy that the j_{corr} values of all the MAO films are significantly lower than that of the substrate. Among the films, the j_{corr} of KTF is the least at a value of 0.08 μA/cm^2 and the j_{corr} of NF is the highest at a value of 0.67 μA/cm^2, corroborating with their R_p values. The j_{corr} of all the tested samples decreases in the order S > NF > KF > NaF > KTF, attesting to the fact that the corrosion resistance values of the MAO treated samples are improved considerably compared to that of the untreated substrate. The film developed in the electrolyte solution containing K_2TiF_6 has the highest corrosion resistance compared to all the other

Table 2
Thermodynamic (OCP) and kinetic parameter values of the NF, KF, NaF and KTF films.

Sample code	OCP (mV)	$\lvert\beta_c\rvert$ (mV)	β_a (mV)	j_{corr} (μA/cm^2)	R_p (kohm cm^2)	Corrosion rate (mm/year)
S	−42.6	132.7	189.2	2.78	1.52	1.93E-3
NF	35.3	127.6	160.5	0.67	46.06	1.68E-3
KF	67.9	144.8	102.3	0.21	123.95	1.45E-3
NaF	93.8	94.3	138.8	0.13	187.55	1.39E-3
KTF	136.4	103.7	226.9	0.08	386.30	6.97E-4

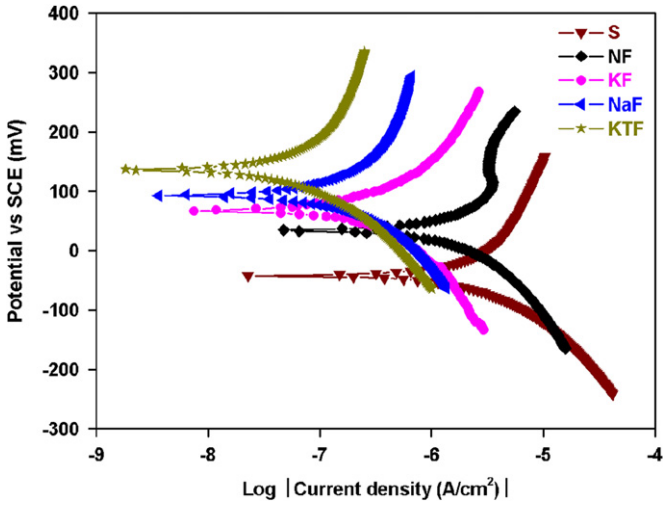

Fig. 7. Tafel polarization curves of the NF, KF, NaF and KTF films in 7.4 pH SBF medium.

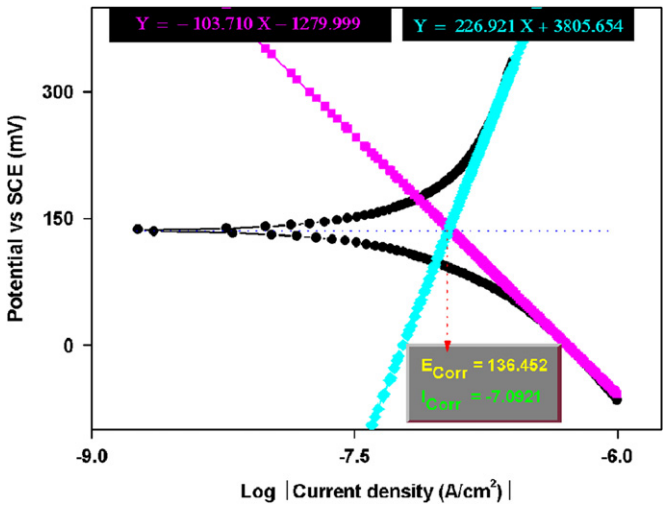

Fig. 8. Tafel extrapolation plot of the KTF film in 7.4 pH SBF medium.

films. Further, the inverse relationship between the corrosion current density values and their respective R_p, is confirmed.

3.6.3. Potentiodynamic polarization studies

The passivation behavior of the substrate and the films was studied by conducting potentiodynamic polarization tests. Fig. 9 depicts the polarization curves of the substrate and the MAO films obtained over a potential range of −500 mV to 3000 mV Vs SCE. It can be observed that all the tested samples exhibit mainly two regions in their anodic sections, namely the active region at lower anodic potentials and the passive region at comparatively higher anodic potentials. In addition, for the substrate 'S' a trans-passive region at a positive potential of about 1400 mV Vs SCE can be observed as shown in Fig. 9. The maximum current densities (j_{active}) of all the test samples attained in their respective active regions is found to decrease in the

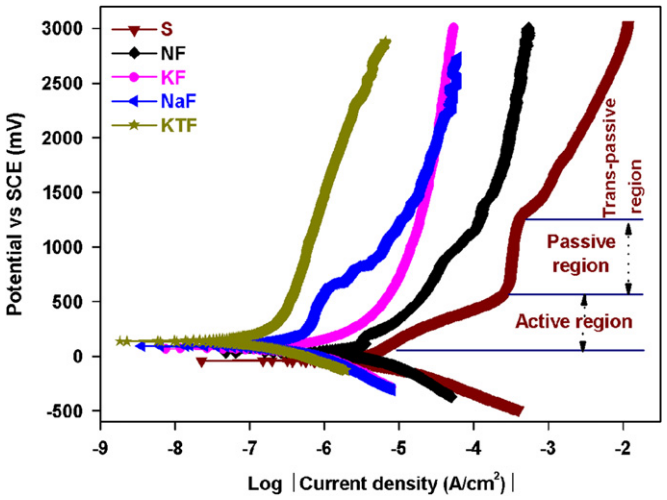

Fig. 9. Potentiodynamic polarization curves of the NF, KF, NaF and KTF films in 7.4 pH SBF medium.

order S > NF > KF > NaF > KTF, which can be attributed to the variations in the rate of metal oxidation process. In fact, the rate of metal oxidation at the metal/oxide interface is strongly influenced by the rate of diffusion of corrosive ions towards the interface and the rate of metal ion transfer away from the metal surface which is further controlled by the resistance offered by the surface oxide film. Thus among the MAO films, the observed least j_{active} of KTF film can be attributed to its highest resistance offered to the diffusion of ionic species due to mainly its less porous structure and higher rutile phase content. Since the rutile titania phase structure is more compact, it offers better corrosion resistance in comparison to anatase titania. Similarly, the observed highest j_{active} of NF film can be attributed to mainly its high porous structure and lower rutile phase content as evidenced by the structural and morphological results of the films reported above. It can also be observed that the anodic current density of the substrate is virtually independent of the sweep potential in the passive region (shown in Fig. 9) which is mainly due to the formation and thickening of a protective oxide layer over its surface. Further, the sudden increase of current density in the trans-passive region is due to the breakdown of the formed protective film and/or due to the evolution of oxygen at sufficiently higher positive potentials. On the other hand, the NF film exhibits an extended active state up to an anodic potential of around 1400 mV and then attains a passive state over the remaining anodic potentials (1400–3000 mV). Similarly, the NaF film shows a passive state in the lower anodic potential region and a comparatively active state at around 750 mV up to 1600 mV and then again shows a passive state over the remaining potential region. This can be attributed to the formation, thickening followed by breakdown at sufficiently higher potentials and subsequent re-passivation of the film formed at the metal–oxide interface. In contrast, the anodic current density of KF film increases gradually with the increase in applied potential and becomes insignificant

above 1500 mV of applied potential. Similarly the anodic current density of KTF film increases slightly over the entire potential region. However, the anodic current density of KTF film is significantly lower than that of all other MAO films and substrate, presumably due to the controlled electrochemical reactions over its surface. It can also be noticed from Fig. 9, that the potentiodynamic polarization curves of KF and KTF have not shown any breakdown indicating that they remain passive almost over the entire range of the applied potential. In summary, the passivation tendency of all the samples is found to decrease in the order KTF > NAF > KF > NF > S which can be attributed to their respective structural and morphological characteristics.

3.6.4. EIS studies

The Bode impedance and phase angle plots of experimental and fitted results for the samples S and NF, KF, NaF and KTF films are presented in Figs. 10(a) and (b) respectively. It can be observed from Fig. 10(a) that the log $|Z|$ of all the test samples decreases with an increase in the frequency. However the frequency vs impedance plots over log scale of all the samples exhibit different features over the low frequency (LF, 0.01–1 Hz) and the high frequency (HF, f > 1 Hz) regions. The impedance of all the films is nearly constant in the LF region and decreases to their respective lowest impedance values at different rates in the HF region. Among the Bode impedance plots, the plot of KTF film exhibits a straight line over the frequency region of 1–10^4 Hz indicating its higher corrosion resistance and capacitive behavior of its outer surface film compared to the other films [27]. The protective behavior of the films is also evident from the near constant phase angle (shown in Fig. 10(b)) in the LF region.

The impedance spectra obtained for uncoated and coated Cp Ti were fitted using electrical equivalent circuit as shown in Figs. 10(c) and (d) respectively and the obtained fitted results are presented in Table 3. The various circuit elements such as resistor and capacitor were checked in different series and parallel combinations to obtain a best fit of the experimental data with the least possible errors. In the fitting procedure, instead of a pure capacitance, a constant phase element (CPE) is used for taking the surface inhomogeniety factor into consideration to get a better fit. The fitting quality was evaluated by the chi-squared values (χ^2) which are of the order of 10^{-3}–10^{-4} as shown in Table 3. Fig. 10(c) clearly indicates the presence of one CPE in parallel to the polarization resistance (*Rp*) and in series with the solution resistance (*Rs*) due to the presence of passive oxide layer over the surface of uncoated Cp Ti. The presence of a passive film over the surface of uncoated Cp Ti is also evident from the OCP and potentiodynamic polarization studies. On the other hand, the equivalent circuit for all the MAO films as shown in Fig. 10(d) consists of two time constants namely CPE_o with a resistor (R_o) in parallel, corresponding to the high frequency characteristics of the outer porous layer

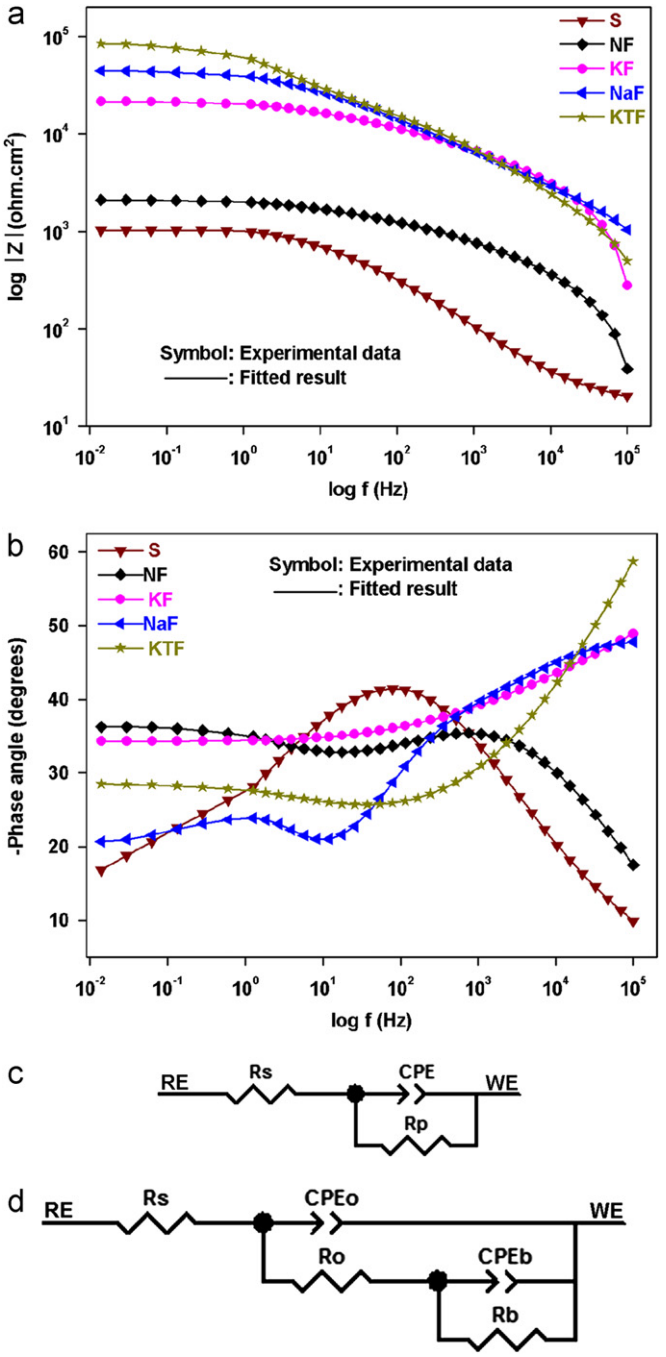

Fig. 10. Experimental and fitted results of Bode impedance (a), phase angle (b) and equivalent circuit for the substrate (c) and circuit for the NF, KF, NaF and KTF films (d).

and CPE_b with a resistor (R_b) in parallel, corresponding to the low frequency characteristics of inner barrier layer of the films. This suggests that the corrosion process is controlled by the charge transfer phenomena. It can be observed from Table 3 that for all the films, the resistance (R_o) of the outer porous layer is small compared to that of their inner barrier layer indicating that the outer porous layer does not contribute significantly to the corrosion protection of the substrate. The resistance of the inner

Table 3
Various electrical parameter values obtained from the equivalent circuit fitting of the EIS data for the substrate (S) and NF, KF, NaF and KTF films.

Sample code	R_s (Ω cm^2)	CPE_o-T	CPE_o-P	R_o (Ω cm^2)	CPE_b-T	CPE_b-P	R_b (Ω cm^2)	χ^2
S	21	–	–	–	6.68E-5	0.66	1.25E3	1.4E-3
NF	31	1.47E-5	0.49	1.15E2	1.94E-6	0.21	4.73E3	3.4E-4
KF	27	1.01E-5	0.54	5.58E2	2.74E-7	0.37	3.79E4	3.6E-3
NaF	35	3.97E-6	0.30	6.10E2	1.76E-7	0.40	5.92E4	4.2E-4
KTF	23	1.93E-6	0.47	9.26E2	1.18E-7	0.61	8.17E4	2.4E-3

barrier layer (R_b) of the films decreases in the order KTF > NaF > KF > NF. It has been reported that the corrosion resistance mainly depends on the inner barrier layer of the film which is in direct contact with the substrate [28]. As KTF has shown the highest R_b value (Table 3) compared to that of all others, it exhibits better corrosion resistance as evidenced by all the electrochemical tests namely OCP, potentiodynamic and EIS tests conducted in the present study.

Based on the results of all the electrochemical corrosion tests conducted in SBF medium, it becomes evident that the KTF film fabricated in the electrolyte solution containing K_2TiF_6 exhibits better corrosion resistance due to mainly its less porous surface structure, stable inner barrier layer and higher rutile phase content. On the other hand, the higher porosity and lower rutile phase content might have mainly contributed to the higher corrosion rate of NF film. Though the high surface porosity of NF film is beneficial to provide mechanical interlocking between the implant surface and the surrounding tissue, it can be detrimental for the implant corrosion resistance and limits the effective life time of the implant in the body fluid environment. Hence an optimal porosity level can make the implant best suit for the intended application. In the present study, the KTF film with significant level of porosity over its surface and with better corrosion resistance can fulfill the requirements of an implant compared to the other films. In addition, the KTF film also contains an appropriate amount of F in its surface structure which can facilitate the better performance of the implant material. Thus the electrolyte solution comprising of 5 g TSOP + 2 g KOH + 3 g K_2TiF_6 is preferable for the development of electrochemically stable F-TiO_2 films on Cp Ti for implant applications.

4. Conclusions

From the present investigation it can be concluded that the use of different electrolyte solutions, comprising of various fluoride containing compounds namely NH_4F, KF, NaF and K_2TiF_6 has resulted in a variation of the structural, morphological, rate of film growth and corrosion characteristics of MAO films on Cp Ti as follows:

The NH_4F containing electrolyte solution resulted in a more porous surface structure with the least stable barrier layer which subsequently led to its highest corrosion rate among the films.

Though the electrolytes containing KF and NaF resulted in a similar morphology, the presence of NaF promoted the anatase to rutile phase transformation at a higher rate compared to that of KF. Further, the NaF containing solution comparatively inhibited the incorporation of P and F into the film during the film growth process.

On the other hand, the K_2TiF_6 containing solution resulted in the highest rutile content and a more stable barrier layer compared to all the other films. The results confirm that the KTF film with sufficient content of F (3 at%) in its surface structure and with highest corrosion resistance compared to all the other films can serve as a successful implant material. Additionally, of all the electrolyte solutions employed in the present study, the one comprising 5 g TSOP + 2 g KOH + 3 g K_2TiF_6 was found to optimal for the fabrication of corrosion resistant F-TiO_2 films on Cp Ti.

Acknowledgments

The authors gratefully acknowledge the financial support from the Department of Biotechnology, New Delhi (BT/PR-11731/MED/32/99/2008, dated 19-08-2009) and the collaborative research project sanctioned by UGC-Networking Resource Centre for Materials, Department of Materials Engineering, Indian Institute of Science, Bangalore, for carrying out this research investigation.

References

[1] P.C. Rath, L. Besra, B.P. Singh, S. Bhattacharjee, Titania/hydroxyapatite bi-layer coating on Ti metal by electrophoretic deposition: characterization and corrosion studies, Ceramics International (2012)http://dx.doi.org/10.1016/j.ceramint.2011.12.026.
[2] H. Liu, J. Xiao, W. Zhong, L. Wang, M. Qi, X. Ying, K. Nakano, T. Kawakami, G. Ma, In vitro behavior of bacteria on fluoride ioncorted titanium: with special regands on porphyromonas gingivalis, Journal of Hard Tissue Biology 20 (2011) 47–52.
[3] H.Y. Liu, X.J. Wang, L.P. Wang, F.Y. Lei, X.F. Wang, J. Ai, Effect of fluoride-ion implantation on the biocompatibility of titanium for dental applications, Applied Surface Science 254 (2008) 6305–6312.
[4] L.F. Cooper, Y. Zhou, J. Takebe, J. Guo, A. Abron, A. Holmen, J.E. Ellingsen, Fluoride modification effects on osteoblast behavior

and bone formation at TiO_2 grit-blasted c.p. titanium endosseous implants, Biomaterials 27 (2006) 926–936.
[5] S.F. Lamolle, M. Monjo, S.P. Lyngstadaas, J.E. Ellingsen, H.J. Haugen, Titanium implant surface modification by cathodic reduction in hydrofluoric acid: surface characterization and in vivo performance, Journal of Biomedical Materials Research Part A 88A (2009) 581–588.
[6] J.E. Ellingsen, Pre-treatment of titanium implants with fluoride improves their retention in bone, Journal of Materials Science: Materials in Medicine 6 (1995) 749–753.
[7] R. Bhola, S.M. Bhola, B.M.D.L. Olson, The role of fluoride ions on the corrosion of Ti36 in normal saline solution as applied to dental implant, International Journal of Electrochemical Science 5 (2010) 917–930.
[8] A.L. Yerokhin, X. Nie, A. Leyland, A. Matthews, Characterisation of oxide films produced by plasmaelectrolytic oxidation of a Ti–6Al–4V alloy, Surface and Coatings Technology 130 (2000) 195–206.
[9] L.R. Krishna, G. Poshal, G. Sundararajan, Influence of electrolyte chemistry on morphology and corrosion resistance of micro arc oxidation coatings deposited on magnesium, Metallurgical and Materials Transactions A 41A (2010) 3499–3508.
[10] L. Rama Krishna, K.R.C. Somaraju, G. Sundararajan, The tribological performance of ultra-hard ceramic composite coatings obtained through microarc oxidation, Surface and Coatings Technology 163–164 (2003) 484–490.
[11] F. Ren, Y. Ling, J. Feng, The role of W doping in response of hydrogen sensors based on MAO films, Applied Surface Science 256 (2010) 3735–3739.
[12] S. Cheng, D. Wei, Y. Zhou, H. Guo, Characterization and properties of microarc oxidized coatings containing Si, Ca and Na on titanium, Ceramics International 37 (2011) 1761–1768.
[13] K. Venkateswarlu, N. Rameshbabu, A.C. Bose, V. Muthupandi, S. Subramanian, D. MubarakAli, N. Thajuddin, Fabrication of corrosion resistant, bioactive and antibacterial silver substituted hydroxyapatite/titania composite coating on Cp Ti, Ceramics International 38 (2012) 731–740.
[14] T. Kokubo, H. Takadama, How useful is SBF in predicting in vivo bone bioactivity?, Biomaterials 27 (2006) 2907–2915
[15] Metals Test Methods and Analytical Procedures, Annual book of ASTM Standards, 3.02, Section 3, ASTM International, Philadelphia, 1987.
[16] D. Sreekanth, N. Rameshbabu, K. Venkateswarlu, Effect of various additives on morphology and corrosion behavior of ceramic coatings developed on AZ31 magnesium alloy by plasma electrolytic oxidation, Ceramics International (2012)http://dx.doi.org/10.1016/j.ceramint.2012.02.040.
[17] J. Liang, B. Guo, J. Tian, H. Liu, J. Zhou, W. Liu, T. Xu, Effects of $NaAlO_2$ on structure and corrosion resistance of microarc oxidation coatings formed on AM60B magnesium alloy in phosphate–KOH electrolyte, Surface and Coatings Technology 199 (2005) 121–126.
[18] J.M. Albella, I. Montero, J.M. Martinez-duart, A theory of avalanche breakdown during anodic oxidation, Electrochimica Acta 32 (1987) 255–258.
[19] H.F. Guo, M.Z. An, H.B. Huo, S. Xu, L.J. Wu, Microstructure characteristic of ceramic coatings fabricated on magnesium alloys by micro-arc oxidation in alkaline silicate solutions, Applied Surface Science 252 (2006) 7911–7916.
[20] K. Venkateswarlu, N. Rameshbabu, D. Sreekanth, A.C. Bose, V. Muthupandi, N.K. Babu, S. Subramanian, Role of electrolyte additives on in-vitro electrochemical behaviour of micro arc oxidized titania films on Cp Ti, Applied Surface Science 258 (2012) 6853–6863.
[21] G. Sundararajan, L.R. Krishna, Mechanisms underlying the formation of thick alumina coatings through the MAO coating technology, Surface and Coatings Technology 167 (2003) 269–277.
[22] A. Ghasemi, V.S Raja, C. Blawert, W. Dietzel, K.U. Kainer, The role of anions in the formation and corrosion resistance of the plasma electrolytic oxidation coatings, Surface and Coatings Technology 204 (2010) 1469–1478.
[23] X.L. Zhang, Zh.H. Jiang, Zh.P. Yao, Zh.D. Wu, Electrochemical study of growth behaviour of plasma electrolytic oxidation coating on Ti6Al4V: effects of the additive, Corrosion Science 52 (2010) 3465–3473.
[24] M.M. Viana, V.F. Soares, N.D.S. Mohallem, Synthesis and characterization of TiO_2 nanoparticles, Ceramics International 36 (2010) 2047–2053.
[25] Y. Wang, B. Jiang, T. Lei, L. Guo, Dependence of growth features of microarc oxidation coatings of titanium alloy on control modes of alternate pulse, Materials Letters 58 (2004) 1907–1911.
[26] M. Karthega, S. Nagarajan, N. Rajendran, In vitro studies of hydrogen peroxide treated titanium for biomedical applications, Electrochimica Acta 55 (2010) 2201–2209.
[27] U. Raghunandan, D. Florian, G. Michael, B. Bikramjit, In vitro corrosion and mineralization of novel Ti–Si–C alloy, Electrochimica Acta 56 (2011) 3809–3820.
[28] A. Ghasemi, V.S. Raja, C. Blawert, W. Dietzel, K.U. Kainer, Study of the structure and corrosion behavior of PEO coatings on AM50 magnesium alloy by electrochemical impedance spectroscopy, Surface and Coatings Technology 202 (2008) 3513–3518.